

# Supplemental Material for “Metamaterial-enabled wireless and contactless ultrasonic power transfer and data transmission through a metallic wall”

Jun Ji<sup>1,\*</sup>, Hyeonu Heo<sup>1,\*</sup>, Jiaxin Zhong<sup>1,\*</sup>, Mourad Oudich<sup>1,2,†</sup>, and Yun Jing<sup>1,‡</sup>

<sup>1</sup>Graduate Program in Acoustics, The Pennsylvania State University, University Park, Pennsylvania, 16802, USA

<sup>2</sup>Université de Lorraine, CNRS, Institut Jean Lamour, F-54000 Nancy, France

February 4, 2024

## Contents

<b>1 The impact of loss factor of SUS316L on the power transmission rate in simulations</b>	<b>2</b>
<b>2 The impact of the number of unit cells on the power transmission rate in simulations</b>	<b>2</b>
<b>3 The impact of the incident angle on the power transmission rate in simulations</b>	<b>3</b>
<b>4 Power transmission enhancement through <math>t = 1\text{ mm}</math> SUS316L wall in air around 50 kHz</b>	<b>3</b>
<b>5 The impact of the fabrication errors on the resonance frequency and power transmission rate in simulations</b>	<b>5</b>
<b>6 Characteristics of the transmitter</b>	<b>5</b>
<b>7 The impact of the transmitter-sample distance on the power transmission rate in simulations</b>	<b>6</b>
<b>8 The measurement of transmitted pressure field</b>	<b>6</b>
<b>9 Characteristics of the receiver</b>	<b>7</b>
<b>10 Design of the energy harvesting circuit</b>	<b>8</b>
<b>11 The power transmission rate in simulations and measurements</b>	<b>9</b>
<b>12 The surface impedance analysis</b>	<b>10</b>
<b>References</b>	<b>12</b>

\*

†

‡

## 1 The impact of loss factor of SUS316L on the power transmission rate in simulations

To evaluate how loss factor of SUS316L affects the power transmission rate in COMSOL, four different typical values are considered:  $\eta = 0.0001$ ,  $\eta = 0.0005$ ,  $\eta = 0.001$ , and  $\eta = 0.002$ . In the simulations, one unit cell is considered under a normally incident wave, and "Continuity" under "Periodic Condition" is applied to both water and SUS316L since there is no wave components along the  $x$  and  $y$  direction. The loss factor is applied under "Damping" of "Linear Elastic Material". The simulated results in Figure S1 indicate that the typical loss factor of SUS316L barely affects the power transmission rate.

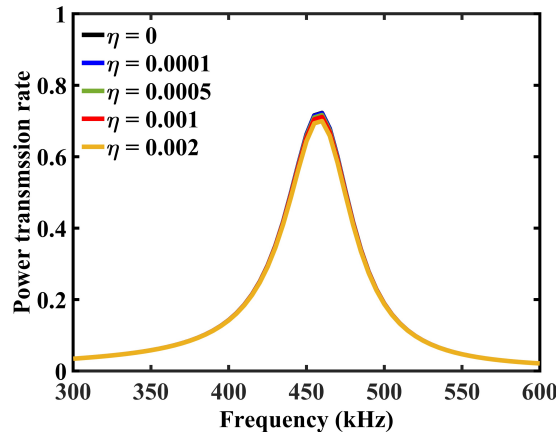


Figure S1: The power transmission rate as a function of SUS316L loss factor in COMSOL.

## 2 The impact of the number of unit cells on the power transmission rate in simulations

To evaluate how the number of unit cells affects the power transmission rate in COMSOL, three different cases are considered:  $6 \times 6$ ,  $10 \times 10$ , and  $20 \times 20$  unit cells. The size of pillar units in Fig. 2c is maintained the same so that the frequency of the vertical elongation mode and the frequency of the peak power transmission are the same for the scenarios of different number of unit cells. The comparison here is to evaluate how the number of pillar units affects the power transmission if attached on a infinitely large metallic plate. The incident wave is a plane wave normal to the plate surface using "Plane Wave Radiation", and the plate is infinitely large to ignore the backward propagation from the edges by setting "Perfectly Matched Layer" around the plate. The incident and transmitted wave are confined in a waveguide having the same cross sectional area with the metamaterial units to ignore the wave diffraction effect. Only  $3 \times 3$ ,  $5 \times 5$ , and  $10 \times 10$  unit cells are modeled in COMSOL with "Symmetry" boundary condition to reduce computational costs. "Perfectly Matched Layer" is set at the transmission end to reduce the back reflection. The non-perfect plane wave from the transducer effect, the finite plate size effect and the wave diffraction effect are considered in the large sample test in Figure S6. Figure S2 shows the pressure distribution for the three cases at the power transmission peak frequency 460 kHz.

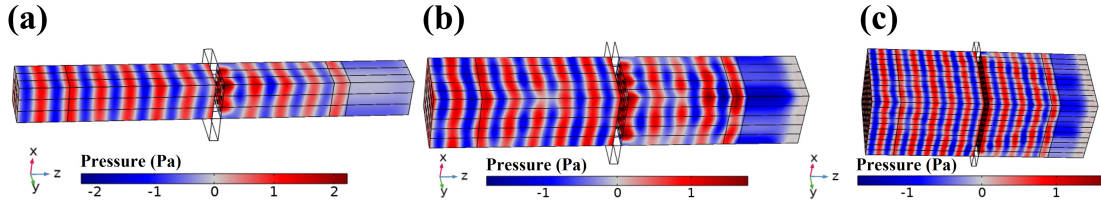


Figure S2: The pressure distribution at the power transmission peak frequency 460 kHz for a)  $6 \times 6$ , b)  $10 \times 10$ , and c)  $20 \times 20$  unit cells. The middle part without the pressure distribution is the plate region simulated with "Solid Mechanics" module.

### 3 The impact of the incident angle on the power transmission rate in simulations

To evaluate how the angle of incidence  $\theta$  affects the power transmission rate in COMSOL, we have chosen the case of  $20 \times 20$  units for illustration. Since we have assumed  $\phi = 0$ , there is no wave component along the  $y$  direction. Therefore, we have constructed only one unit cell along the  $y$  direction, with "Continuity" under "Periodic Condition" being applied to both water and SUS316L along the  $y$  direction to reduce computational costs. The incident wave is applied using "Background Pressure Field" with a parametric sweep of  $\theta$  from  $0^\circ$  to  $60^\circ$  and the scattered field can be solved from 300 kHz to 600 kHz. "Perfectly Matched Layer" is applied at both the incident and transmitted sides to minimize reflections. The transmitted power is calculated by integrating the default function "Acoustic Intensity" along a surface enclosing the metamaterial at the transmitted side. Figure S3a and Figure S3b illustrate the distribution of the background pressure and the scattered pressure, respectively, when the excitation frequency is 460 kHz and  $\theta = 60^\circ$ . And a strong transmission can be observed.

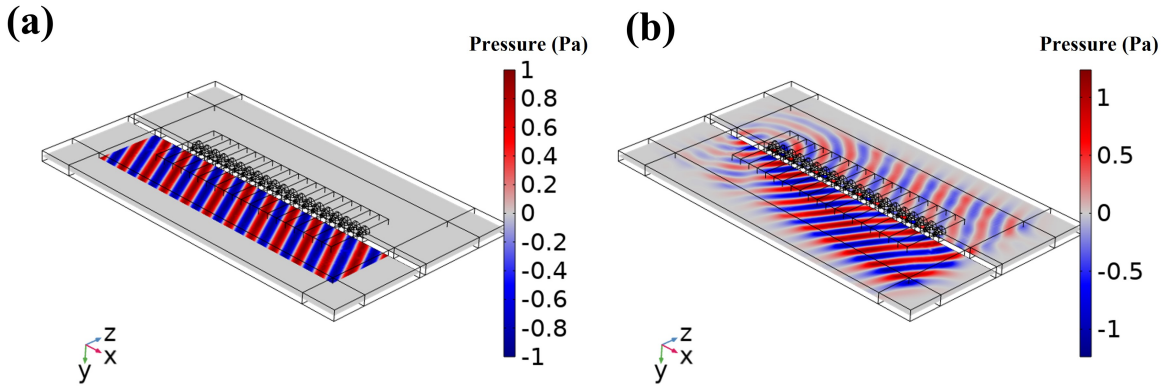


Figure S3: The distribution of a) the background pressure and b) the scattered pressure when the excitation frequency is 460 kHz and  $\theta = 60^\circ$ .

### 4 Power transmission enhancement through $t = 1$ mm SUS316L wall in air around 50 kHz

To demonstrate the generality of the design philosophy of power transmission enhancement, a double-sided pillar-based acoustic metamaterial is proposed to enhance ultrasonic power transmission through 1 mm thick SUS316L plate in air, with a 50 kHz ultrasound as the incident wave, as shown in Figure S4a. Considering the huge impedance mismatch between air and SUS316L, identical pillars are distributed

on both sides of the plate to induce a larger vibration for power transmission enhancement. The same procedure with band structure and transmission analyses is utilized to design the metamaterial. The only difference from the water scenario is that the background medium of air is not considered in the band structure calculation since the mass loading effect from air is very small. Consequently, the obtained band structure is purely real. The size of the unit cell is  $p = 5.72$  mm (less than one wavelength at 50 kHz),  $t = 1$  mm,  $d_s = 0.42$  mm,  $d_m = 5.43$  mm,  $h_s = 0.86$  mm,  $h_{m1} = 1.15$  mm, and  $h_{m2} = 6.14$  mm. Figure S4b and Figure S4c show the band structure and the power transmission for a unit cell with Floquet periodic condition, respectively. The vertical elongation mode at 50.92 kHz shown in the inset contributes to the power transmission rate enhancement from 0.00001% to near 100% around 51 kHz. Unlike the water-SUS316L case, the air-SUS316L case is ultra-sensitive to the loss factor of SUS316L, as shown in Figure S4d. As the loss factor increases, the peak power transmission rate near 51 kHz is decreased by several orders of magnitude, which is 94%, 20%, 2%, 0.6%, and 0.15% when the loss factor is 0, 0.0001, 0.0005, 0.001, and 0.002, respectively. However, the power transmission rate for the loss factor of 0.002 is still 4 orders of magnitude higher than that without AMM. The nature of being ultra-sensitive to the loss factor and the narrow bandwidth are likely caused by the huge impedance mismatch between the air and SUS316L, which requires more advanced 3D additive metal printing in the future for experimental validations.

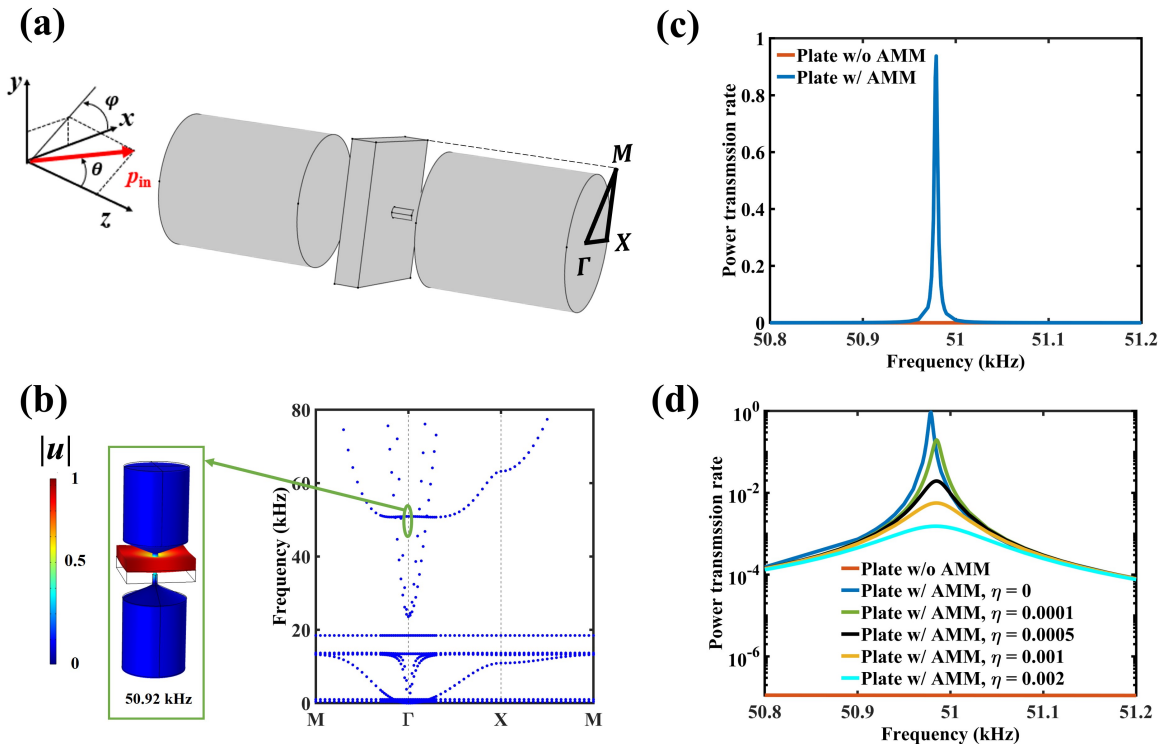


Figure S4: Design of the double-sided pillar-based metamaterial for the power transmission enhancement through a 1 mm metal plate in air at 50 kHz. a) Schematic of a periodically arranged unit cell under a incident plane wave and the first irreducible Brillouin zone. b) Band structure. c) Power transmission rate for the plate w/ and w/O AMM under a normally incident plane wave. d) The typical loss factor of SUS316L significantly affects the power transmission rate.

## 5 The impact of the fabrication errors on the resonance frequency and power transmission rate in simulations

The impact of fabrication errors on the resonance frequency of a pillar is illustrated in Figure S5. The upper section of the figure shows symmetric (Fig.S5a) and asymmetric (Fig.S5b) pillar shapes, highlighting the influence of asymmetry on the resonance frequency and maximum power transmission rate (Fig.S5c). The lower section of the figure presents an isometric view (Fig.S5d) and a cross-sectional view (Fig.S5e) of a non-flat profile cone-shaped pillar. 3D bar graphs depict the variation of the resonance frequency (Fig.S5f) and the maximum power transmission rate at resonance frequencies (Fig.S5g) with geometric tolerance parameters such as the height ( $h$ ) and width ( $w$ ) of the cone shape. The degree of asymmetry does not affect the resonance frequency as long as the mass cylinder is shifted within 2.5% of the mass diameter. Furthermore, the maximum power transmission rate remains unaffected, with changes of less than 0.02%. Although there is relatively noticeable deviation in resonance frequency and power transmission rate due to geometric tolerance, the variations are still acceptable. The non-flat profile cone-shaped pillar exhibits less than 2% and 3% variations in resonance frequency and power transmission rate, respectively, underscoring its robustness.

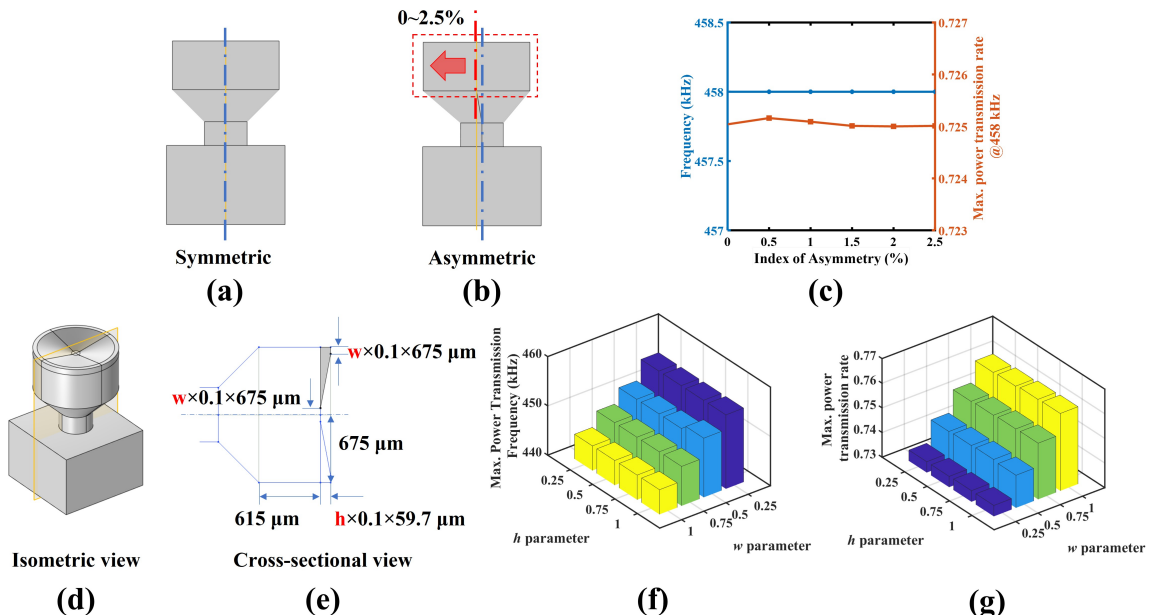


Figure S5: Impact of fabrication errors on the resonance frequency of a pillar and its power transmission rate. (Top) (a) Symmetric and (b) asymmetric shapes. (c) Resonance frequency and power transmission rate (at 458 kHz) affected by degree of asymmetry. (Bottom) (d) Isometric and (e) cross-sectional views. (f) Resonance frequency and power transmission rate bars at resonance frequencies dependent on tolerance parameters,  $h$  and  $w$ , of the cone shape, respectively.

## 6 Characteristics of the transmitter

The on-axial pressure field of the unbaffled 1 inch transducer is simulated in COMSOL, and it is compared with the analytical prediction [1] for a baffled piston source at 460 kHz as shown in Figure 3e. The transducer is modeled by imposing “Incident Pressure Field” under “Plane Wave Radiation” on a circle with a diameter of 1 inch. The locations of the multiple local extremes in the near field are matched with the predictions, while the magnitude of the normalized pressure is slightly different from the predictions,

which is mainly caused by the unbaffled condition.

## 7 The impact of the transmitter-sample distance on the power transmission rate in simulations

A series of large sample simulations are conducted to model the real experimental scenarios. Only  $10 \times 10$  unit cells are modeled in COMSOL with "Symmetry" boundary condition to reduce computational costs, and a workstation with 1 TB memory is used to run the simulations. The non-perfect plane wave from the transducer effect, the finite plate size effect and the wave diffraction effect are considered in the following ways: 1) The transducer is modeled by imposing "Incident Pressure Field" under "Plane Wave Radiation" on a quarter of the circle with a diameter of 1 inch. 2) "Fixed Constraint" under "Solid Mechanics" is imposed on the corner of the plate to modal the sample holder in experiments. 3) "Perfectly Matched Layer" is set at the surroundings to reduce the back reflection like the anechoic absorbing layer in experiments.

To evaluate how the transmitter-sample distance  $d_{tm}$  affects the power transmission rate in COMSOL, two extreme cases in Figure 3e are considered:  $d_{tm} = 14$  mm in which the plate is placed at the far-est maximum on-axial pressure point, and  $d_{tm} = 9.1$  mm in which the plate is placed at the minimal on-axial pressure point. Figure S6a shows that the power transmission rate is almost the same for both cases. At the peak power transmission frequency of 460 kHz, a strong transmission can be attained with AMM, as depicted in the pressure distribution for both cases in Figure S6b.

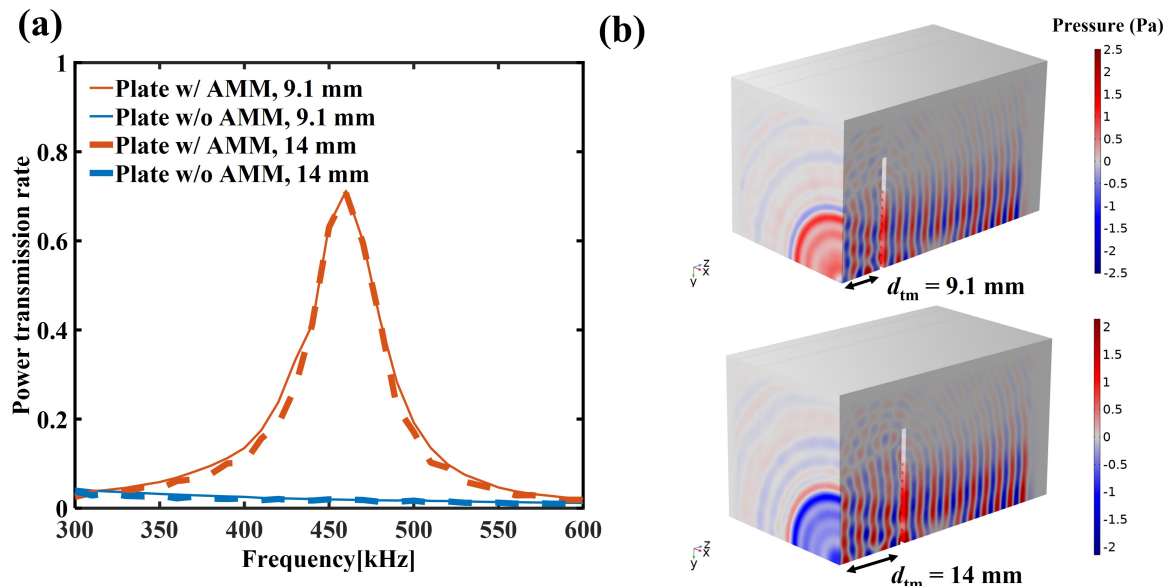


Figure S6: a) The power transmission rate when the plate is placed at the minimal/maximal pressure location in the near field of the transmitter ( $d_{tm} = 9.1$  mm/ 14 mm). b) The pressure distribution for "Plate w/ AMM" at 460 kHz .

## 8 The measurement of transmitted pressure field

Figure S7 illustrates the emitted and received signals by the transducer and hydrophone, respectively, in both the time and frequency domains for various cases. The emitting signal comprises five cycles in each

burst, with a frequency of 445 kHz, and the burst period is 1 ms. Here, the signal received at a spatial point located at  $(x, y, z) = (0, 0, 45 \text{ mm})$  is presented as an example.

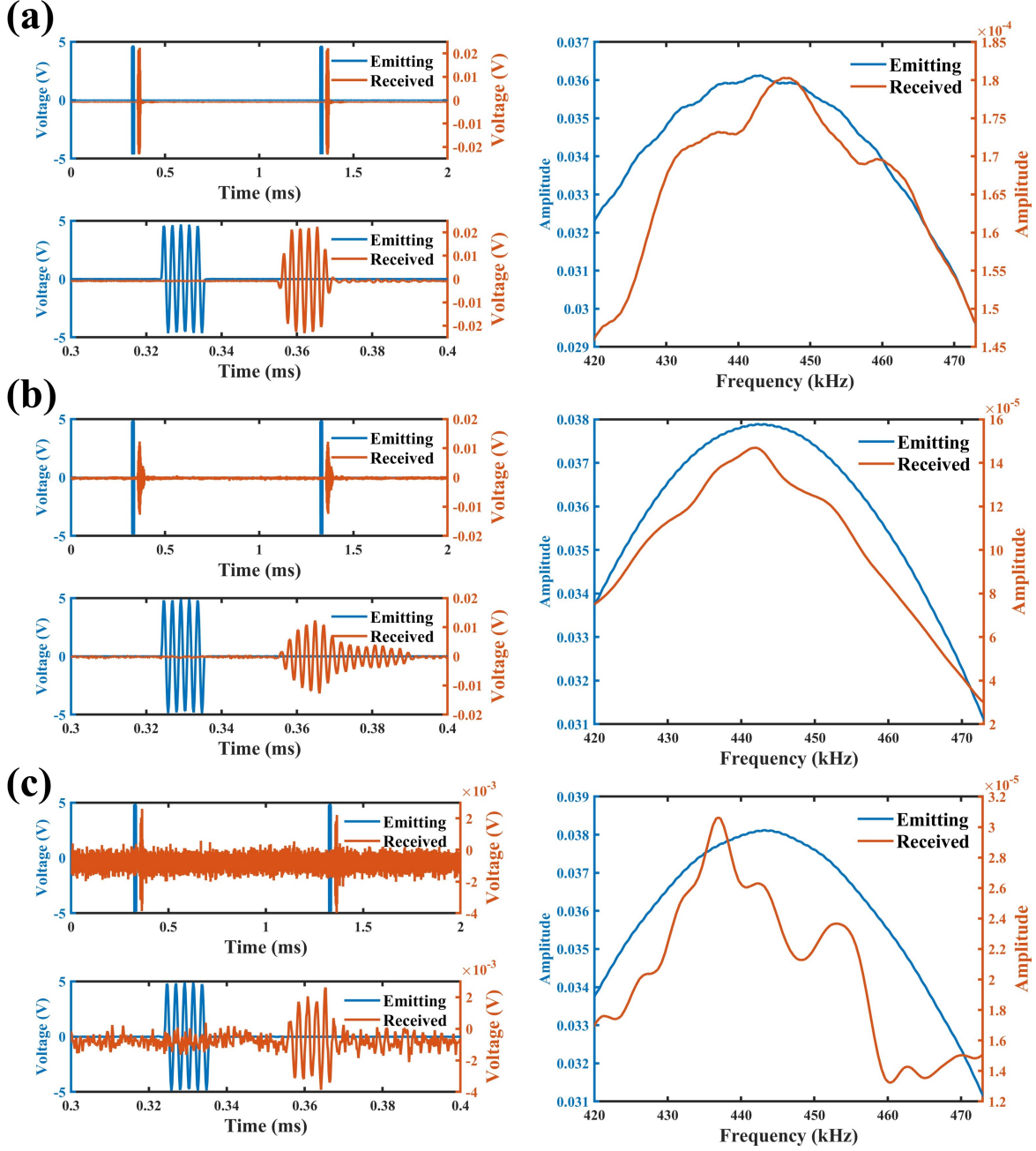


Figure S7: The measured emitting and received signals in the time domain (left column) and frequency domain (right column) for three cases: a) “No plate”, b) “Plate w/ AMM”, and c) “Plate w/o AMM”. For time signals, the top panel displays two periods of the burst and the bottom panel displays the zoomed-in signals.

## 9 Characteristics of the receiver

Figure S8a shows the measured impedance of the 1.5 inch receiver with a resonant frequency around 400 kHz. The magnitude of the measured impedance is  $300 \Omega$  at 460 kHz. Next, the optimal power transfer from the receiver to a resistive load is demonstrated in Figure S8b. Different load resistances (

from  $50 \Omega$  to  $1 \times 10^6 \Omega$ ) are connected in series to the receiver, when the 1 inch transmitter is driven by a continuous-mode ultrasound at 460 kHz (which is close to the frequency we are interested to harvest energy). As the load resistance increases, the measured output voltage on the resistor shows a rising tendency and saturates at a higher external load. The instantaneous power output of the receiver is also estimated by  $(V_{pp}^2/(4Z_L))$  [2], where  $V_{pp}$  is the peak-to-peak output voltage on the resistive load  $Z_L$ . The instantaneous power output reaches the maximal at an external load of  $325 \Omega$ , which has a good match with the measured impedance magnitude of the receiver  $300 \Omega$  at 460 kHz. The results indicate that the power transfer can be optimal when the impedance between the receiver and the load is matched.

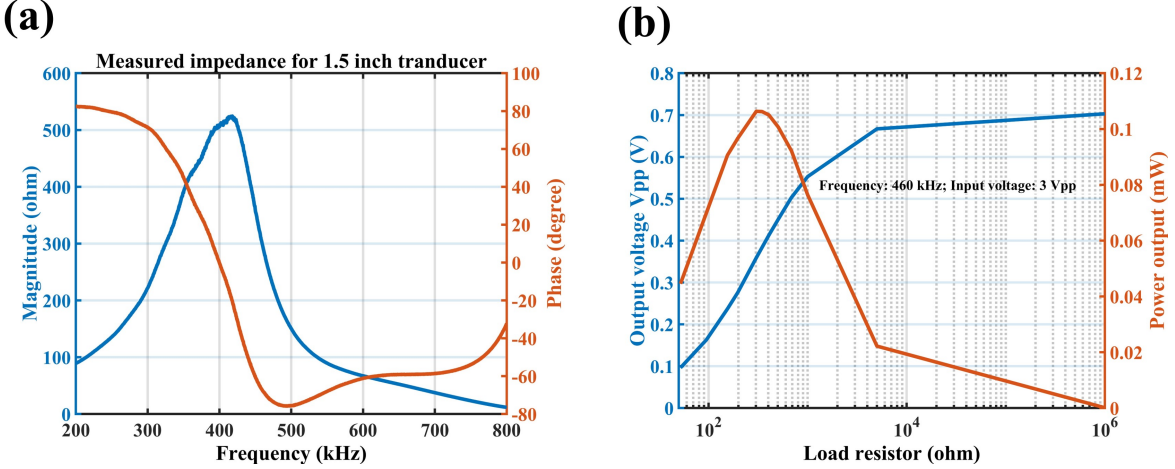


Figure S8: a) The measured impedance of the receiver. b) The output voltage and power from the receiver to a series-connected resistive load, respectively, showing an optimal output power at  $325 \Omega$ .

## 10 Design of the energy harvesting circuit

In this work, a circuit has been designed for energy harvesting. The schematic diagram of the circuit is depicted in Fig. S9. It is implemented on a two-layer printed circuit board (PCB). The traces of the top and bottom layers are shown in Fig. S10(a) and (c), respectively. The 3D rendering of the PCB and a top-view photo are presented in Fig. S10(b) and (d), respectively. As shown in Fig. S10, the PCB can be divided into several functional sections. The top of the PCB houses 9 relays (HUI KE HK19F-DC9V-SHG) that are utilized to switch the wiring for capacitors. Additionally, the middle of the PCB has 10 slots for  $220 \mu\text{F}$  through-hole capacitors. Below the slots is a full bridge rectifier comprising of 4 Schottky diodes (IN5711), and a through-hole red LED is located below the rectifier. The right side of the PCB is equipped with two BNC connectors; the one labeled ‘‘INPUT’’ is connected to the receiving transducer, while the other labeled ‘‘OUTPUT’’ is connected to an oscilloscope. On the left side of the PCB, there is a DC power barrel jack that provides power to the relays. Three switches are located at the bottom left of the PCB. The ‘‘SW\_WIRING’’ switch is utilized for switching the wiring of capacitors, the ‘‘SW\_CHARGE’’ switch is used for toggling the charging process, and the ‘‘SW\_LED’’ switch is used for powering the LED. The designed circuit facilities a more convenient experiment implementation of the energy harvesting compared to existing circuits (e.g., [2]).

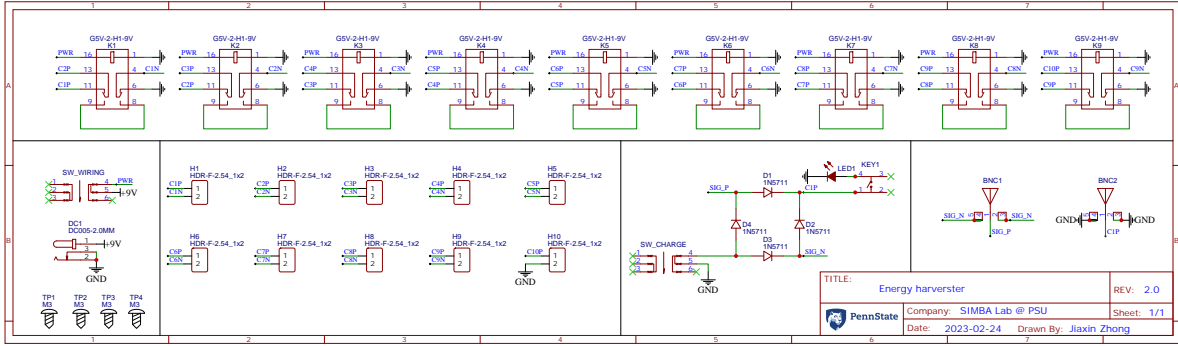


Figure S9: Schematic diagram for the energy harvesting circuit.

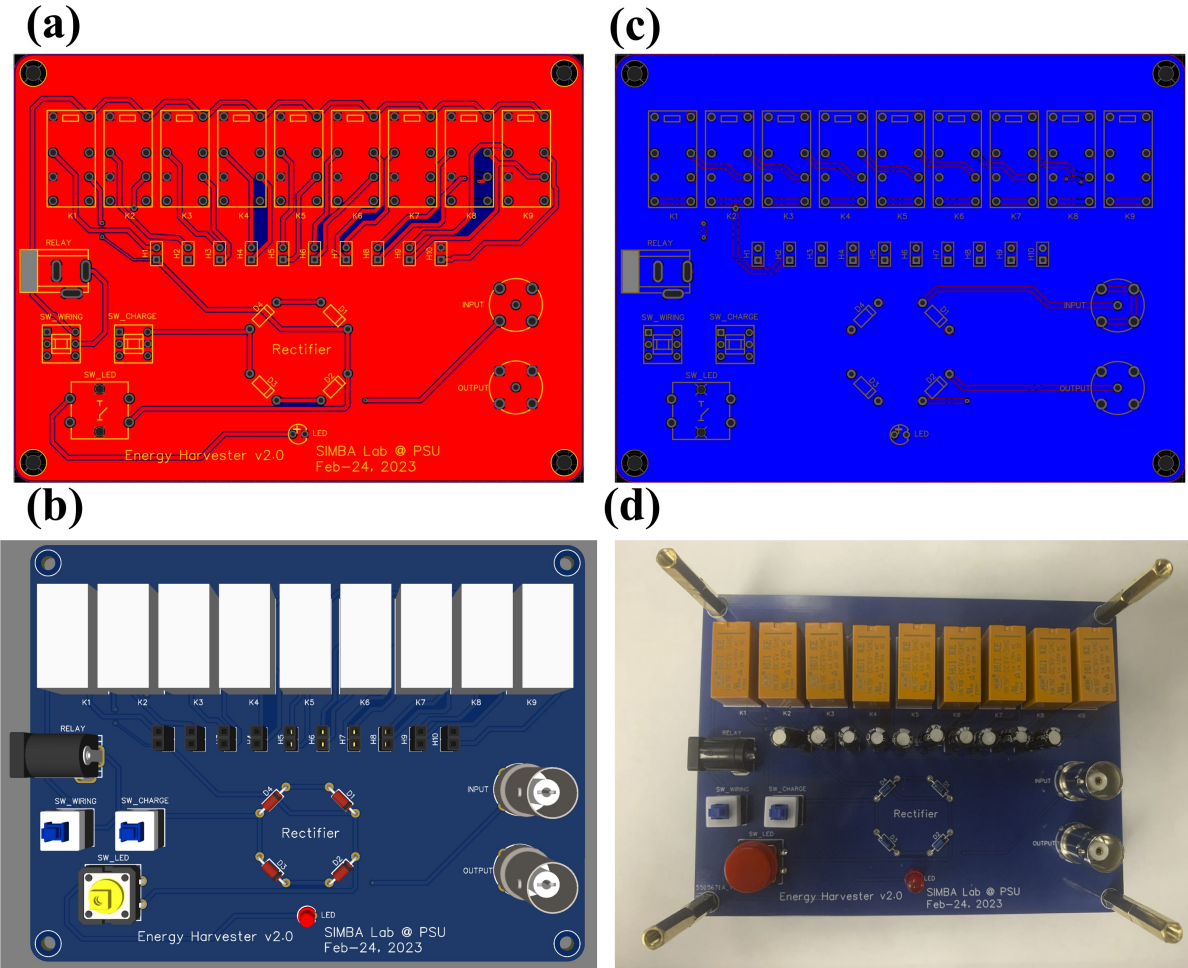


Figure S10: The traces of the circuit on a) the top layer and b) the bottom layer of the PCB. c) 3D rendering and d) the photo of the PCB.

## 11 The power transmission rate in simulations and measurements

In simulations, the power transmission  $T$  is rigorously calculated by the surface integral of acoustic intensity (a default vector variable in COMSOL,  $\mathbf{I} = (\text{acpr.lx}, \text{acpr.ly}, \text{acpr.lz})$ ) at the transmission side

in COMSOL. The expression for the intensity is,

$$I = \frac{1}{2} \operatorname{Re} \{ p v^* \}$$

We integrate this quantity, for example, along the surface  $S$  indicated in Figure S11 for normal and oblique incidence (Please refer to notes S2 and S3 in the supplementary material),

$$T = \int_S I dS$$

Consequently, the power transmission rate is  $T_{\text{AMM}}/T_{\text{NoPlate}}$  and  $T_{\text{NoAMM}}/T_{\text{NoPlate}}$  for “Plate w/ AMM” and “Plate w/o AMM” scenarios, where  $T_{\text{AMM}}$ ,  $T_{\text{NoAMM}}$  and  $T_{\text{NoPlate}}$  are the power transmission in the case of “AMM”, “No AMM” and “No Plate”, respectively.

In measurements (Fig. 3(f) in the manuscript), the power transmission  $T$  is approximated by the surface integral of  $|p|^2/(2\rho_0 c_0)$  at a plane of  $z = 45\text{mm}$  from the metamaterial plate, which is a reasonable plane-wave approximation (as supported by the pressure distribution shown in Figs. 4(c) and 4(d)) when transitioning to the far field. The power transmission rate is then calculated using  $T_{\text{AMM}}/T_{\text{NoPlate}}$  and  $T_{\text{NoAMM}}/T_{\text{NoPlate}}$  for “Plate w/ AMM” and “Plate w/o AMM” scenarios. Two observations support our approximation. First, the measured pressure field is very similar to the simulated field in both x-y plane and x-z plane, both of which indicate the far field transition around  $z = 45\text{mm}$  as we calculated in Fig. 3(e). Second, the approximated power transmission rate (using  $\int_{z=45\text{mm}} \frac{|p|^2}{2\rho_0 c_0} dS$ ) has a good agreement with the exact power transmission rate (using  $\int_{z=45\text{mm}} \text{acpr.lz} dS$  in COMSOL) in simulation as shown in Figure S12. Consequently, it is reasonable to approximate the power transmission rate in experiments by using the formula,

$$\int_{z=45\text{mm}} \frac{|p|^2}{2\rho_0 c_0} dS$$

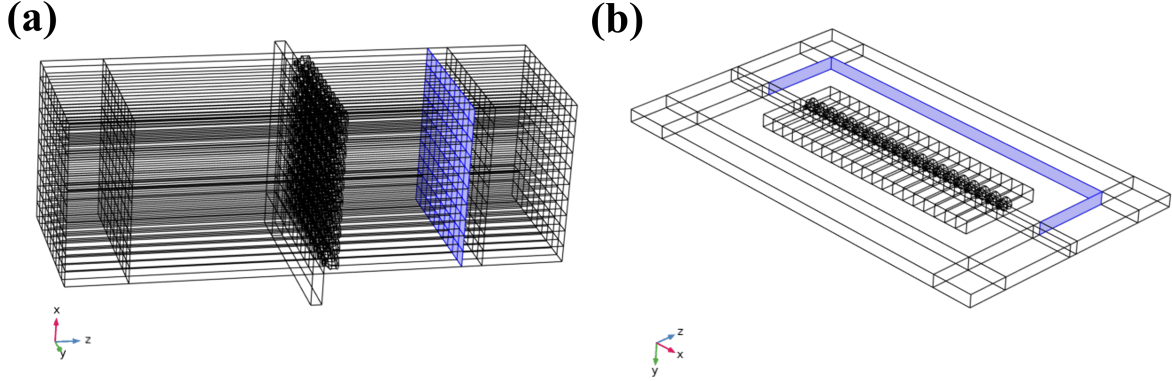


Figure S11: The surface (highlighted in blue) on which the integral of acoustic intensity is conducted for a)the evaluation of the number of unit cell in Note S2 with  $20 \times 20$  units, b)the evaluation of the incident angle in Note S3.

## 12 The surface impedance analysis

The homogenization theory [3, 4], which uses effective material parameters to characterize acoustic metamaterials with sub-wavelength unit cells, loses its effectiveness for our unit cell with dimensions around the working wavelength ( $p \approx 0.46\lambda_0$  and the height is around  $0.7\lambda_0$ ). To demonstrate how the pillars change the impedance of the metallic plate, the surface impedance  $Z_{\text{surf}}$  at the surface of

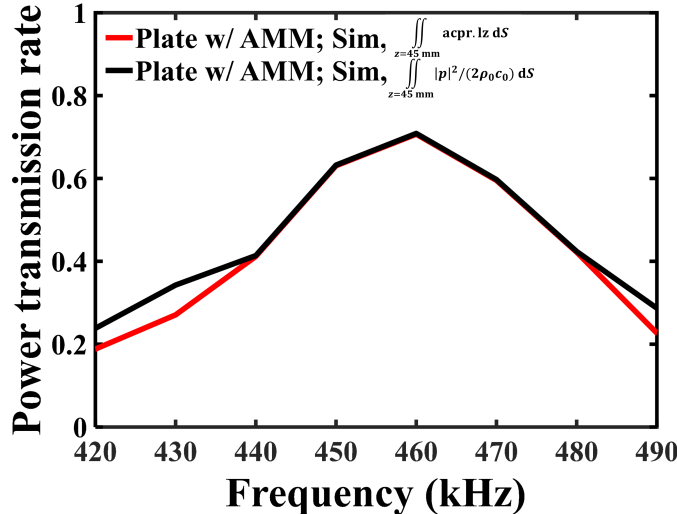


Figure S12: Two methods in COMSOL to calculate the power transmission rate in the case of “Plate w/ AMM”. The proposed approximation using  $\int_{z=45\text{mm}} \frac{|p|^2}{2\rho_0 c_0} dS$ , and the exact method using  $\int_{z=45\text{mm}} \text{acpr.lz} dS$ . A good agreement between two methods shows that the approximation is reasonable in simulation.

the metallic plate, where the incident wave impinges perpendicularly ( $\theta = 0^\circ, \phi = 0^\circ$ ), is probed in COMSOL by the average of the acoustic pressure divided by the average of the normal acoustic velocity, as shown in Figure S13a. The normalized surface impedance gets closer to 1 around 460 kHz. The power reflection coefficient can be reconstructed from the normalized surface impedance  $z_{\text{surf}} = Z_{\text{surf}}/(\rho_0 c_0)$  as  $R = |\frac{z_{\text{surf}} - 1}{z_{\text{surf}} + 1}|^2$ . Consequently, the power transmission is  $T = 1 - R$ , since the loss is negligible as shown in Note S1. Figure S13b shows a good agreement between the recontacted transmission and the actual transmission(probed using a default variable acpr.lz), which confirms the validation of the surface impedance method.

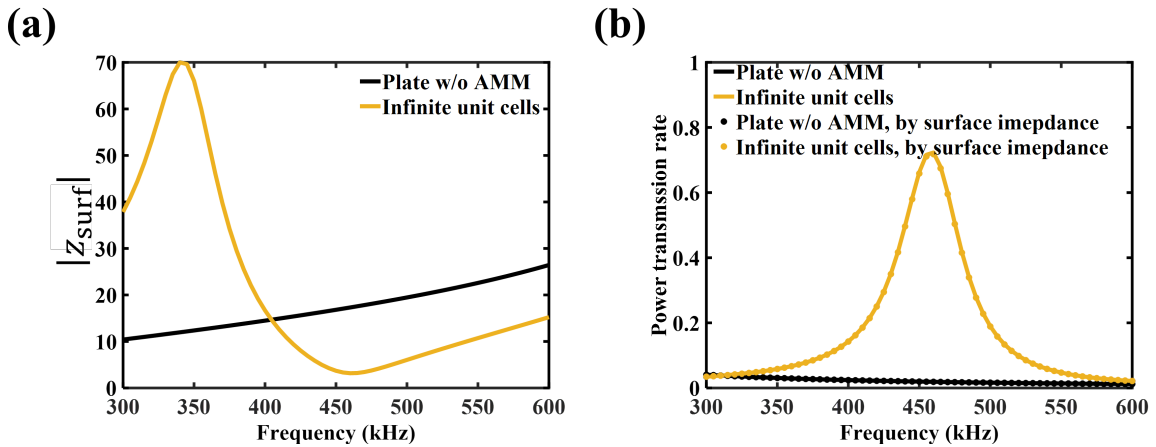


Figure S13: a)The surface impedance  $Z_{\text{surf}}$  at the surface of the metallic plate, where the incident wave impinges perpendicularly ( $\theta = 0^\circ, \phi = 0^\circ$ ), is probed in COMSOL by the average of the acoustic pressure divided by the average of the normal acoustic velocity. b)The power transmission rate that is probed using a default variable acpr.lz in COMSOL(solid lines) and reconstructed by the surface impedance(dot markers).

## References

- [1] Lawrence E Kinsler, Austin R Frey, Alan B Coppens, and James V Sanders. *Fundamentals of acoustics*. John wiley & sons, 2000.
- [2] Laiming Jiang, Yang Yang, Ruimin Chen, Gengxi Lu, Runze Li, Jie Xing, K Kirk Shung, Mark S Humayun, Jianguo Zhu, Yong Chen, et al. Ultrasound-induced wireless energy harvesting for potential retinal electrical stimulation application. *Advanced Functional Materials*, 29(33):1902522, 2019.
- [3] Bogdan-Ioan Popa and Steven A Cummer. Design and characterization of broadband acoustic composite metamaterials. *Physical Review B*, 80(17):174303, 2009.
- [4] Vladimir Fokin, Muralidhar Ambati, Cheng Sun, and Xiang Zhang. Method for retrieving effective properties of locally resonant acoustic metamaterials. *Physical review B*, 76(14):144302, 2007.